Experimental investigation and modelling of a 1.5 kW axial turbine for waste heat recovery of a gasoline passenger car through a Rankine cycle

Olivier Dumont[a], Mouad Diny[b], Vincent lemort[c]
[a] Thermodynamics laboratory, Liege, Belgium, olivier.dumont@ulg.ac.be
[b] PSA GROUPE, La Garenne Colombes, France, mouad.diny@mpsa.com
[c]Thermodynamics laboratory, Liege, Belgium, Vincent.lemort@ulg.ac.be

Abstract

The Rankine cycle power system is a promising technology to convert the wasted thermal energy from engines into useful energy. In a way to decrease the CO_2 emissions of passenger cars, it is possible to recover the waste heat from the exhaust gas that presents a high exergy compared to other sources of waste heat (engine cooling, exhaust gas recovery cooling, etc.). A Rankine cycle test-rig is designed and built to assess the performance of such a cycle in real operating conditions. The most critical component is the expander. This component needs to be compact, light, efficient, reliable and cheap among other criteria. In this context, a 1.5 kW axial turbine composed of two wheels is tested on a Rankine cycle test-rig coupled with a 150 kW engine. A detailed analysis of the performance is proposed. The maximum turbine mechanical isentropic efficiency reached is 41.5%. A semi-empirical approach is proposed to predict the performance of the axial turbine in a wide range of conditions. Finally, the performance on a driving cycle is compared with another technology of expander (scroll).

Introduction

According to the EU 2050 Roadmap (European Climate Foundation, 2010), greenhouse gases emissions (GHG) could be cut by 80% in 2050. In this context, Rankine cycle systems are useful to recover waste heat from different applications (industry process, internal combustion engines, etc.) or to produce combined heat and power from biomass.

In literature, small scale Rankine cycles (power < 20 kW) are seldom but can be found. In 2006, three scroll compressors modified to run as expanders were tested and presented maximum isentropic efficiencies of 55% [1]. A 5 kW Rankine cycle for biomass application was developed in 2010 [2]. In 2010, a non-lubricated scroll (modified scroll) reached an efficiency of 48% with a nominal power close to 1 kW [3]. In 2013, a 5 kW solar Rankine cycle, using a mono piston expander, was tested with parabolic trough collectors [4]. In 2015, a two-wheel axial turbine (10 kW) was tested for CHP applications [5]. This shows that the knowledge about Rankine cycle systems presenting a small power (<10kW) is still limited nowadays. Finally, in 2014 a prototype of non-lubricated scroll expander, designed to work at high temperature, presented an isentropic efficiency of 28% [6]. Because of the scarce literature regarding this topic, the purpose of the present work is to characterize and model the behavior of one of the most important components of the Rankine cycle, which is the expander. The considered expander is a 1.5 kW axial steam turbine, selected because of its high energy density and low cost.

After a short introduction, the experimental facility and the semi-empirical model are described (Methodology). In section three (Results), the experimental results are presented together with the calibration of the semi-empirical model. A discussion about the turbine performance is proposed based on the semi-empirical model (section four). This section also proposes a comparison of performance with a scroll expander on a driving cycle. A few conclusions and perspectives are drawn in the last section.

Methodology

Experimental facility

The test bench is shown schematically in Figure 1 and is composed of a gasoline engine (A) as heat source. The power of the latter is dissipated in a brake (not shown). The exhaust gases are directed towards the evaporator (B), which can be bypassed if necessary, before being evacuated. Concerning water, it is stored in a tank (C) at atmospheric pressure. At the outlet of the latter, water is filtered before passing into the feed pump (D) and is then directed towards the evaporator (B). The feed pump is controlled by a frequency inverter in to adjust the shaft speed between 380 and 3000 RPM.

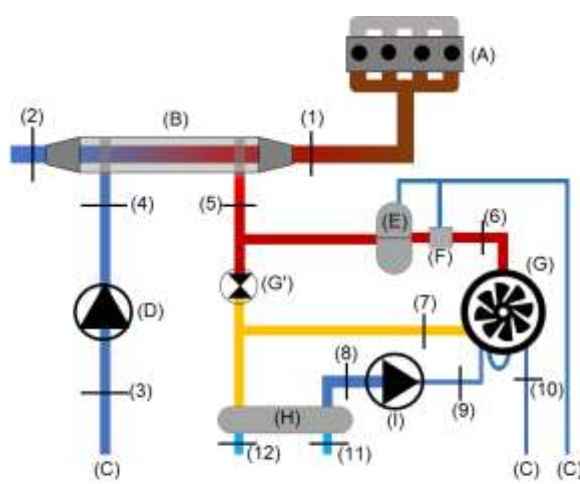

Figure 1. Layout of the test-rig.

Then, thermally insulated pipes direct it to the turbine (G) via two accessories: the trap (E) and the separator (F), allowing any condensates to be evacuated. The turbine can also be bypassed by a valve (G') for start and stop procedures. At the outlet of the turbine, the water is pumped through the condenser (H) by means of a vacuum pump (I) placed downstream. The latter allows to simulate the pressure that would be reached in a closed cycle. It then passes through the turbine again, for the purpose of cooling the integrated electric generators, and is finally returned to the tank (C). In order to control the system, the manipulated variables are the speed and torque imposed to the motor, the shaft speed of the feed pump (D), the opening of the bypass valve (G') and the electrical resistance imposed to the turbine generators. Since the latter are asynchronous generators, the resistance imposed on them determines their speed of rotation, hence that of the turbine.

The action turbine is composed of two wheels without any stator (Figure 2).

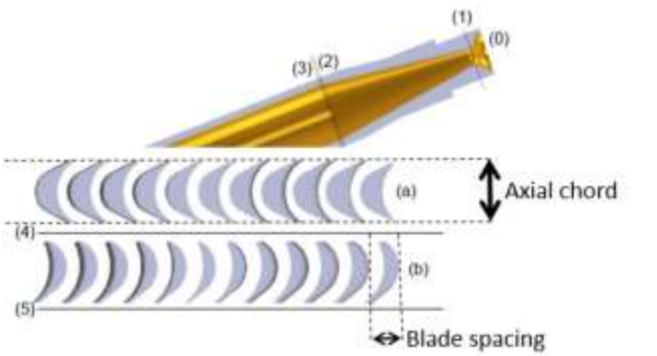

Figure 2. Diagram of the nozzle and blade wheels and notations.

The reason to use a second stator is to recover the remaining power of the fluid after passing through the first wheel, which can be useful, particularly in part load conditions. Its characteristics are listed in Table 1. The generators of the turbine (one for each wheel) are connected to AC/DC inverters that are connected to a 90-ohm variable resistance. In this paper, the shaft speed refers to the first wheel, the second wheel rotates at a speed 2.2 times smaller. Figure 3 depicts the energy flow of the turbine.

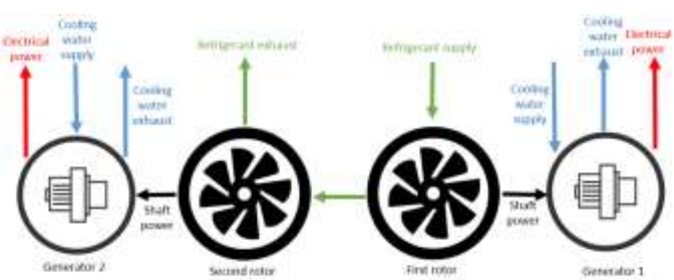

Figure 3. Flowchart diagram of the turbine

Figure 2 shows a detailed view of the two-wheel axial turbine. (0) is the turbine inlet. (1) is the de Laval nozzle throat. The angle of incidence of the nozzle is 70° with respect to the axis of the turbine.

Table 1. Characteristics of the turbine

Parameter	Value
Nominal DC power [W]	1 500
Maximal shaft speed [RPM]	30 000
Nominal supply pressure [bar]	5
Nominal exhaust pressure [bar]	0.05
Maximal temperature [°C]	220
Generator efficiency [%]	92
AC/DC converter efficiency [%]	94

(2) is the end of the divergent part. (3) is also the end of the divergent part, but the conditions that prevail there are those of the body of the turbine. (a) is the first rotor. (4) corresponds to the state of the fluid between the two wheels. (b) is the second rotor. (5) is the turbine outlet. Pressure and temperature measurements are available at this location.

The test-rig is equiped of a large number of sensors. Their characteristics are presented in Table A1 (appedices) with the numbering related to Figure 1. Data is checked and the outliers are eliminated through a Gaussian Process [7].

Semi-empirical modelling

Semi-empirical models rely on a limited number of physically meaningful equations that describe the most influent phenomena within the system. They offer a good trade-off between simulation speed, calibration efforts, modelling accuracy and extrapolation capabilities [8]. Semi-empirical models have extensively been used for the sizing and the modelling of heat exchangers, compressors, expanders and pumps [9-13]).

Three conservation equations are used to model the turbine (mass flow rate (Equation 1), momentum (Equation 2) and total enthalpy (Equation 3).

$$\rho_{in} V_{in} A_{in} = \rho_{ex} V_{ex} A_{ex} \quad (1)$$

$$P_{in} + \rho_{in} V_{in}^2 = P_{ex} + \rho_{ex} V_{ex}^2 \quad (2)$$

$$h_{in} + \frac{V_{in}^2}{2} = h_{ex} + \frac{V_{ex}^2}{2} + \frac{\dot{W}_{rot}}{\dot{m}} \quad (3)$$

The thermodynamic state of the fluid at the throat of the Laval nozzle (Figure 2) is determined assuming a sonic flow, the conservation of the total enthalpy (Equation 3) and the conservation of entropy, assumed because of the small dimensions of the converging part.

$$h_2 = h_{2,is} + k_s \frac{V_2^2}{2} \quad (4)$$

Following this, the thermodynamic properties at the end of the divergent part (Figure 2) are determined assuming the conservation of the mass flow rate (1), the conservation of the total enthalpy (Equation 3) and an entropic loss coefficient (k_s – (Equation 4)), which is a calibration parameter. This models the enthalpic increase produced by an entropy increase.

The shock occurring at the end of the divergent part (Figure 2) is computed with the conservations of the mass flow rate and of the momentum (Equations 1-2).

For the rotor, the second wheel is not modelled since its influence is negligible on the performance of the turbine during normal operation (see section Results). For the first wheel, the three aforementioned laws are applied (Equations 1-3). The rotor power is then evaluated with Euler's relation (Equation 5):

$$\dot{W}_{rot} = \dot{m}(U_a(V_3 \sin(\alpha) - V_4 \sin(\alpha))) \qquad (5)$$

Considering the dimensions of the nozzle relative to those of the impeller and the absence of stator blades, the admission is considered to be partial. There are 3 types of losses in partial admission [14]:

- Windage: the part of the wheel far from the inlet is still immersed in the fluid, which is driven by the wheel in a centrifugal movement leading to losses proportional to U_3.
- Expansion: expansion losses refer to changes in flow rate in the inter-blade channels as they enter or exit the sector of admission, causing loss of momentum.
- Mixing: when an inter-blade channel enters the admission sector, the stagnant fluid it contains is mixed with the fluid arriving at high speed from the nozzle. The mixing itself constitutes an additional loss.

According to [14], the power lost due to the afore-mentioned losses can be expressed as follows (Equation 6)

$$\dot{W}_{loss} = \frac{f \rho U^3}{2} + \frac{K}{1+K} \frac{s \varepsilon_{TT} \dot{m} U^2}{3 \pi D \varepsilon \sigma_{is}^2} \qquad (6)$$

In (Equation 6), f is a coefficient equal to 1.4, ρ is the density, U is the mean absolute speed of the blades, K is the velocity coefficient, s is the blade spacing (Figure 2), ε_{TT} is the ratio of the actual total enthalpy drop to the isentropic enthalpy drop, $\dot{m}$ is the mass flow rate, D is the diameter of the wheel at mid-height of the blades, ε is the fractional arc of admission, σ_{is} is the second velocity coefficient [14].

Apart from the windage, expansion and mixing losses from (Equation 6), leakage losses are modelled with a coefficient characterising the proportion of flow bypassing the blades (k_f) and electrical losses are taken into account with the generator and rectifier efficiency (Table 1).

To summarize, the models presents four inputs (supply pressure, shaft speed, exhaust pressure and superheating), two calibration parameters (entropic loss coefficient (k_s) and proportion of flow bypassing the blades (k_f)), four geometrical parameters (axial chord (b), blade spacing (s), diameter of the wheel (D) and fractional arc of admission (ε)). The two outputs are the mechanical power and the mass flow rate. Figure 4 depicts the flowchart of the semi-empirical model of the turbine.

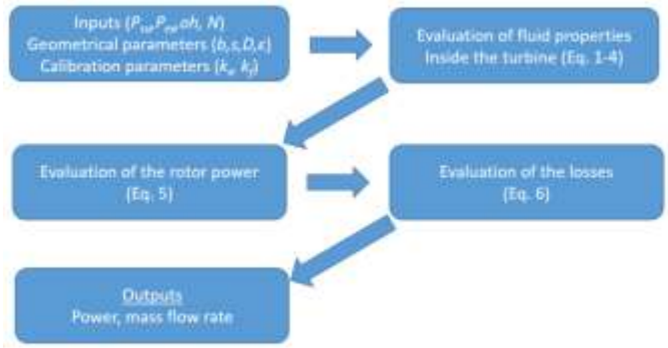

Figure 4. Flowchart of the semi-empirical model.

Engine modelling

The engine model is a confidential polynomial law predicting the cooling engine thermal power, the exhaust gas mass flow rate and temperature based on the torque and the shaft speed of the vehicle.

Results

Range of operating condition

A total of 105 steady-state measurements have been achieved (Table 2). In order to cover the operating conditions of the turbine, its shaft speed and the temperature of the exhaust gases are varied within the limitation of the turbine.

Table 2. Range of operating conditions

Parameter	Range
Supply temperature [°C]	[119:196]
Exhaust pressure [bar]	[0.189:0.322]
Supply pressure [bar]	[1.8:7.2]
DC power [W]	[99.4:1438]
Mass flow rate [g/s]	[2.7:8.5]
Shaft speed [RPM]	[4 600:29 810]

Example of T-s diagram

Figure 5 depicts an example of T-s diagram corresponding to the measurement point with the highest electrical production. The fluid follows the following path: (1) condenser exhaust, pump supply, pump exhaust (ex cd), (2) cooling supply (su cooling), (3) cooling exhaust (ex cooling), (4) evaporator supply, (5) evaporator exhaust (ex ev), (6) turbine supply (su tu), (7) turbine exhaust and condenser supply (ex tu) and finally back to the condenser exhaust (1).

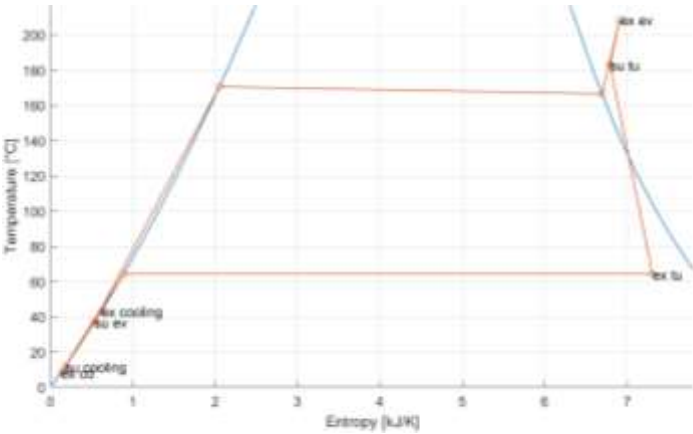

Figure 5. T-s diagram of the maximum output power measurement. Blue is the saturation curve of water, orange is the T-s diagram of the Rankine cycle.

Performance

A common indicator for a turbine is the reduced mass flow rate (Equation 7) in function of the pressure ratio (Equation 8).

$$\dot{m}_{red} = \frac{\dot{m}\sqrt{t_{exp,ex}}}{P_{exp,ex}} \qquad (7)$$

$$pr = \frac{P_{exp,su}}{P_{exp,ex}} \qquad (8)$$

Figure 6 shows the linear trend between the pressure ratio over the turbine and the reduced mass flow rate. Changing the shaft speed ([4 600:29 810] RPM) of the turbine does not affect the mass flow rate. For a given flow, only one value of pressure ratio is physically reachable. This means that only one control parameter (the working pump speed) is necessary to regulate the Rankine cycle. This is different from volumetric expanders where both the working fluid pump and the expander speed influence the working conditions.

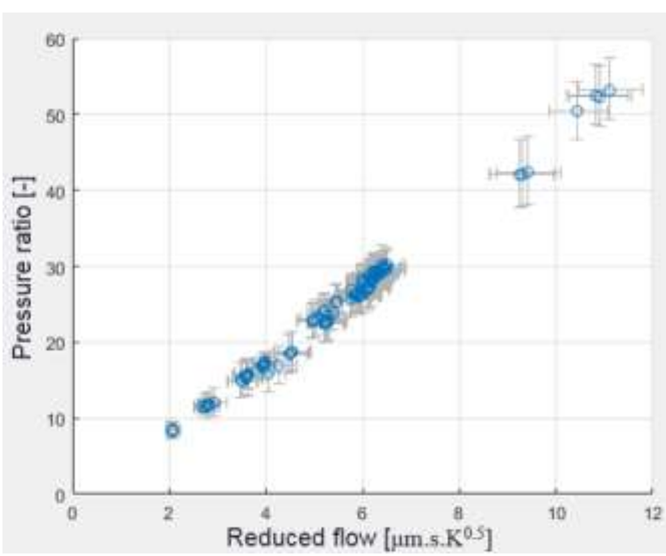

Figure 6. Evolution of the pressure ratio over the turbine with the reduced mass flow rate.

Figure 7 shows the DC power generated in function of the shaft speed and the mass flow rate of working fluid. The power monotonically increases with the mass flow rate and the shaft speed.

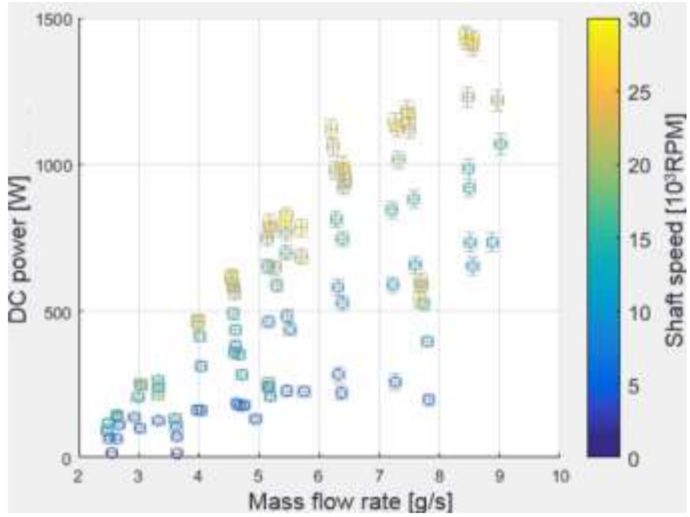

Figure 7. DC power in function of the shaft speed and the mass flow rate.

It is observed that working at the nominal (and maximal) shaft speed (30 000 RPM) leads to the best performance of the turbine (Figure 7). The power generated is measured separately for both wheels. It is observed that the power generated by the second wheel is always lower than 20% of the total power (Figure 8). Moreover, when working with an optimal control (30 000 RPM), the power ratio of the second wheel (compared with the total power) is very low (<3%). This is an indication for the successful lay out of the first wheel. Indicating, that behind the first wheel, there is more or less no angular momentum in the flow, - all work is done in the first stage. Only because the electrical load (resistance) is limited, the shaft speed cannot be increased to its maximum speed. In this case, the second wheel produce a non-negligible amount of power compared to the first wheel.

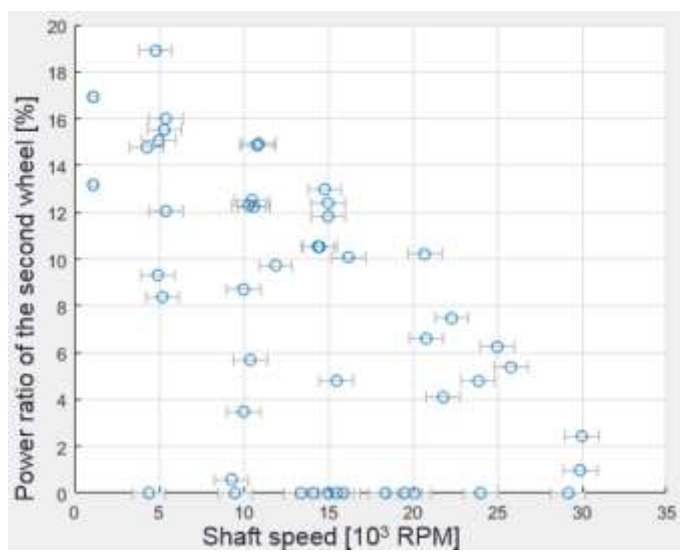

Figure 8. Power ratio of the second wheel.

The mechanical isentropic efficiency is defined by Equation 9 and presented in Figure 9. η_{gen} is the efficiency of the turbine generator while $\eta_{AC/DC}$ is the DC converter efficiency (Equation 8).

$$\eta_{exp,is,mec} = \frac{\dot{W}_{exp,el}}{\dot{m}.\eta_{gen}.\eta_{AC/DC}(h_{exp,in}-h_{exp,ex,is})} \qquad (9)$$

The value of the maximal isentropic mechanical efficiency (41.5%) is rather low compared to typical values for turbines. This result is partly explained since *"very small turbines are intrinsically less efficient because of the increase of secondary and leakage losses"* [15].

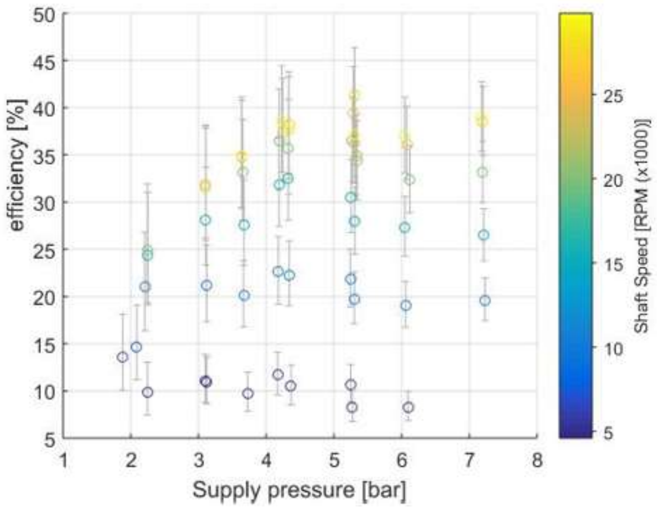

Figure 9. Evolution of the mechanical isentropic efficiency of the turbine with the supply pressure and shaft speed

In the same way as for the generated power (Figure 7), the efficiency is maximal at the nominal maximum shaft speed (30 000 RPM).

Model calibration

Following the description of the model (section methodology), two calibration parameters have to be tuned. A genetic algorithm in software Matlab allows finding the minimum of (Equation 10) and leads to an entropic loss coefficient (k_s) of 0.309 and a proportion of flow bypassing the blades (k_f) of 0.325.

$$\min_{x} f = \sqrt{\sum_i \left(\left(\frac{\dot{m}_{meas,i}-\dot{m}_{pred,i}}{\dot{m}_{meas,i}} \right)^2 + \left(\frac{\dot{W}_{meas,i}-\dot{W}_{pred,i}}{\dot{W}_{meas,i}} \right)^2 \right)} \qquad (10)$$

Figure 10 presents the simulated power versus the measured power (left) and the simulated mass flow rate versus the measured one (right).

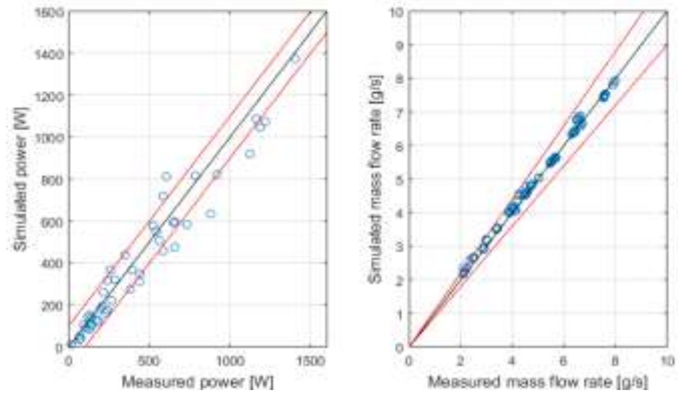

Figure 10. Parity plot for the turbine (left = power (100W error bar), right = mass flow rate (10% error bar)).

Considering the low number of tuned parameters and the relative simplicity of the semi-empirical model, the prediction is considered as satisfying with a mean error of 55 W on the power generation.

Discussion

Now that the semi-empirical model has been calibrated (section Results), it is possible to predict the performance of the turbine in a wide range of conditions based on simulations. Here, the superheating is set to 50 K, the shaft speed to 30 000 RPM, two exhaust pressures. A 50 K overheating is a classical value for a small-scale Rankine cycle to avoid any droplets that could destroy the turbine.

Usually in a passenger car, there is the cooling engine circuit, presenting a temperature around 90°C, and eventually a second circuit working at lower temperature (60°C). In this work, these two temperatures are investigated as exhaust temperature for the turbine, leading to exhaust pressures of respectively of 700 mbars and 200 mbars. Moreover, a third exhaust temperature of 32°C (corresponding to 50 mbars) is also studied because it corresponds to the nominal operating condition of the turbine. The supply pressure is of the turbine is varied between 2 and 8 bar for these three typical exhaust temperatures to see how the power of the turbine is affected. In Figure 11, a continuous increase in the generated power is observed when increasing the supply pressure at constant exhaust pressure. The power is decreased by more than 200 W when increasing the condensation pressure from 50 mbar (32°C) to 200 mbar (60°C). It shows the importance of working in the nominal conditions defined by the manufacturer (Table 1). An exhaust turbine temperature of 90°C is not recommended since the power produced becomes very low (below 400 W).

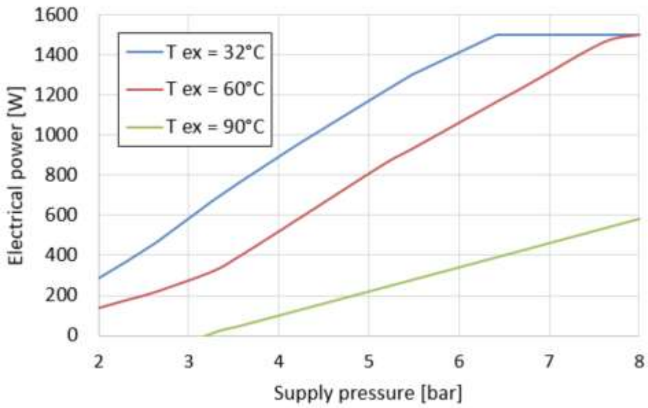

Figure 11. Generated power for different supply pressures and exhaust temperatures.

In Figure 12, the isentropic efficiency is plotted for different supply pressures. Like in Figure 11, three exhaust temperatures are chosen: 32°C which correspond to the nominal exhaust pressure of the turbine, 60°C and 90°C which reflects respectively the most common temperature level of water loops encountered in a passenger car. For the nominal conditions (exhaust pressure of 50 mbar – 32°C), a maximum is observed at the nominal supply pressure (5 bar). However, the power can still be increased with higher supply pressure as shown in Figure 13. On the contrary, at higher exhaust temperatures (200 mbar and 700 mars), no maximum is observed and the efficiency increases monotonically up to the maximum supply pressure close to 8 bar.

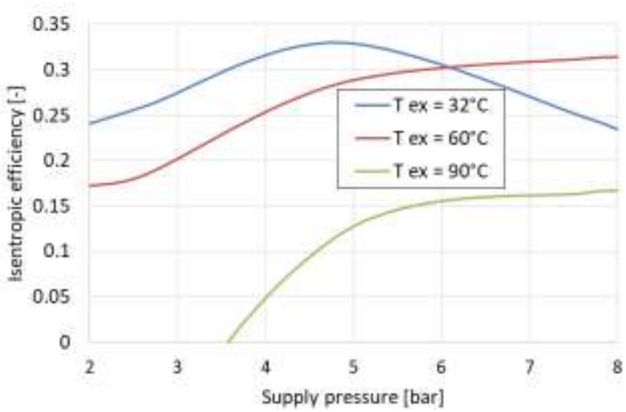

Figure 12. Isentropic efficiency for different supply pressures and exhaust temperatures.

The performance of the turbine is now compared with that of a scroll expander. The simulation is performed with a real scroll prototype (30% nominal efficiency) an optimized theoretical scroll (60% nominal efficiency) and a hybrid current evaporator [16]. The 60% efficiency performance is studied for the scroll because it looks more realistic regarding state of the art. However, no other efficiency is simulated for the turbine since efficiencies are usually low for such small power. The evaporator superheating is fixed to 50K, the sub-cooling is equal to 5 K, the shaft speed of the scroll is optimized to maximize the power and the condensation pressure is equal to one bar if not specified. A 5 K sub-cooling is commonly adopted to avoid cavitation phenomena and while optimizing the cycle efficiency. The performance is compared based on two driving cycles. The New European Driving Cycle (NEDC) (or Motor Vehicle Emissions Group - MVEG), based on a theoretical driving profile, is used in Europe since 1973. From 2017, the Worldwide harmonized Light vehicle Test Cycle (WLTC) should be preferred since the cycle was developed using real-driving data. Figure 13 presents the net electrical production for 6 case studies: The real scroll expander (30% efficiency), the optimal one (60% efficiency) and the turbine with condensation temperature of 60°C and 90°C in each case. The considered torque of the vehicle engine is the average one for a given speed on the WLTP cycle.

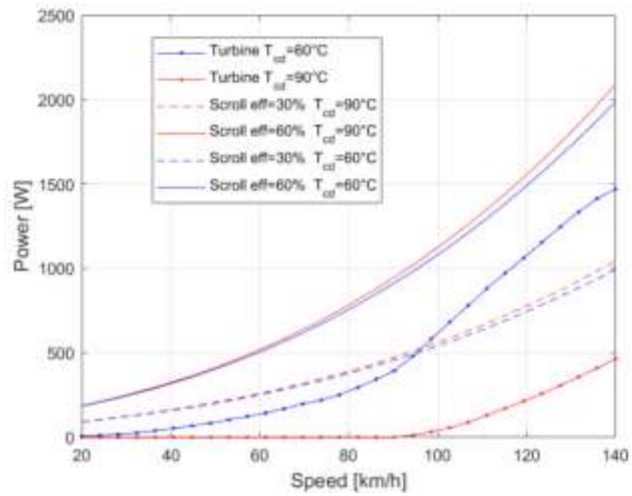

Figure 13. Generated power for both expanders in function of the vehicle speed.

It appears from Figure 13 that the turbine performs better at high vehicle speed. This is due to the thermal content of the exhaust gas that becomes significant only for vehicle speeds above 90 km/h. The scroll expander outperforms the turbine at vehicle speeds below 90 km/h because of a better performance at part load (low thermal power/low pressure ratio's). Also, the turbine performance is very sensitive to the exhaust temperature, unlike the scroll expander (Figure 13).

Figure 14 compares simulation results for the consumption decrease for the four case studies and two driving cycles for "cold start" and "hot start". The cold start takes into account a realistic inertia for the exhaust gases (120 s) and for the cooling engine (600 s) to reach a sufficient temperature before starting the Rankine cycle. Practically, the WLTP cycle is probably th e most representative of the reality even if no cycle can be considered as perfect. Also, the cold start situation is the most realistic because of the representative inertia taken into account. Some car manufacturers use the exhaust gases to heat the cooling engine loop at start, which helps at decreasing the cold start time [17]. If this idea is used, the real solution of the system is located somewhere between the "cold start simulation" and the "hot start simulation". The global improvement of the performance of the engine is evaluated considering the additional weight of the Rankine Cycle (30 kg) and the additional power due to the pumping losses produced by the addition of a heat exchanger in the exhaust gases [18]. In this work, the dynamics effects are neglected, i.e. the models are always used in steady state. Also, a maximum improvement of performance is evaluated assuming that the whole energy produced by the WHRS is useful. From Figure 14, it appears that the turbine produces less energy than the surplus consumption due to the addition of the Rankine cycle. This is due to the high condensation temperature of the system which does not match the nominal conditions of the turbine (Figure 11).

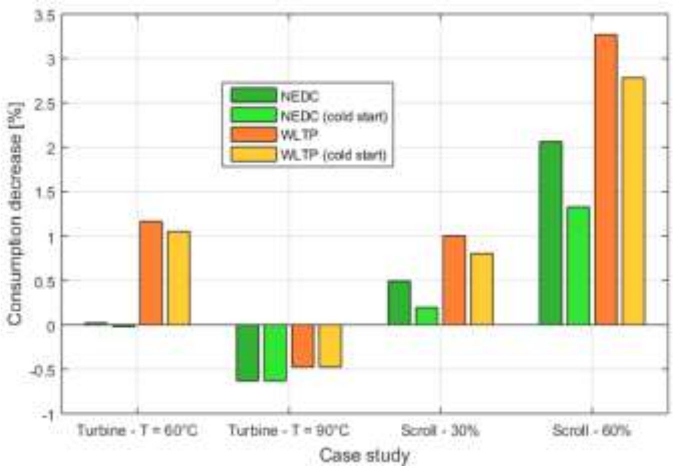

Figure 14. Simulation of the driving cycle performance

Conclusions

This paper studies the possibility of waste heat recovery through a Rankine Cycle. A test-rig is developed to evaluate the performance of a 1.5 kW axial turbine. The maximum mechanical isentropic efficiency reached is 41.5%. A semi-empirical approach is proposed to predict the performance of the axial turbine in a wide range of conditions. The following observations can be drawn:

- To maximize the power generated by the turbine, the latter should spin at its maximal shaft speed (30 000 RPM).
- The second wheel always produces very low amount of power (<3% of the total power) when working at maximal speed.
- Working out of the nominal conditions (exhaust pressure or supply pressure) strongly affects the efficiency of the turbine.

The maximum fuel consumption decrease is equal to 2.7% in the most realistic driving cycle. This value is slightly too low to ensure a substantial economic benefit. It would therefore be necessary to optimize the geometry of the turbine to work with a higher efficiency in the range of working conditions of a passenger car.

References

1. Lemort, V., Teodorese, I. V., Lebrun, J., “Experimental Study of the Integration of a Scroll Expander into a Heat Recovery Rankine Cycle”, 18th International Compressor Engineering Conference, 2006.
2. Boudellal, M., “Cogeneration. Technique and engineering”, ISSN 1624-1843. New industry, Paris : Dunod, France, 2010.
3. Aoun, B., “Micro combined heat and power operating on renewable energy for residential building”, PhD thesis, Paris (France), 2010.
4. Bouvier, J-L., « Étude expérimentale d’une installation de micro-cogénération solaire couplant un concentrateur cylindro-parabolique et un moteur à cycle de Hirn », PhD thesis, 2014.
5. Paulides, J, Post, E., Post, J., Encica, L., Lomonova, E., « Green turbine, a high speed double turbine for sustainable energy harvesting from waste heat”, 2015 Tenth International Conference on Ecological Vehicles and Renewable Energies (EVER), 2015.
6. Legros, A., « Conception d’un expanseur scroll adapté à la récupération d’énergie à l’échappement pour une application automobile : Aspects thermodynamiques et tribologiques », PhD thesis, Liege (Belgium), 2014.
7. Dumont, O., Quoilin, S., Lemort, V., “Importance of the reconciliation method to handle experimental data in refrigeration and power cycle: application to a reversible heat pump/organic Rankine cycle unit integrated in a positive energy building”, International Journal of Energy and Environmental Engineering 2016, 7(2).
8. Dumont, O., Dickes, R., Lemort, V., 2017b. Extrapolability and limitations of a semi-empirical model for the simulation of volumetric expanders , IV International Seminar on ORC Power Systems, ORC2017 13-15 September 2017, Milano, Italy.
9. Lemort, V., “Contribution to the characterization of scroll machines in compressor and expander modes”, PhD thesis, 2008.
10. Quoilin, S., “Sustainable energy conversion through the use of organic Rankine cycles for waste heat recovery and solar applications”, PhD thesis, 2011. (Liege).
11. Declaye, S., “Improving the performance of µ-ORC system”s, PhD thesis, Liège, 2015.
12. Dumont, O., Dickes, R., Lemort, V., “Experimental investigation of four volumetric expanders, IV International Seminar on ORC Power Systems”, ORC2017 13-15 September 2017, Milano, Italy.
13. Dickes, R., Dumont, O., Daccord, R., Quoilin, S., Lemort, V., “Modelling of organic Rankine cycle power systems in off-design conditions: An experimentally-validated comparative study”, Energy 2016, 10.1016/j.energy.2017.01.130.
14. Horlock, J. H., “Axial flow turbines: fluid mechanics and thermodynamics”, Krieger Publishing Company, 1973.
15. Machi, E. Astolfi, M., “Axial flow turbines for Organic Rankine Cycle applications”, Organic Rankine Cycle (ORC) Power Systems Technologies and Applications, 2017.
16. Dumont, O., Legros, A., Diny, M., Lemort, V., “Experimental investigation of the valorization of the exhaust waste heat of a gasoline engine based on a Rankine cycle”. Conference ECOS 2017.
17. Diehl, P., Haubner, F., Klopstein, S., Koch, F., “Exhaust heat recovery systems for modern cars”, Sae technical papers series, SAE World Congress, 2001.
18. Barrieu, E., EHRS Impact on Engine Warm up and Fuel Economy, Directions in engine efficiency and emission research conference, 2011.
19. Pascual, L., “Study of Organic Rankine Cycles for Waste Heat Recovery in Transportation Vehicles”, PhD thesis, 2017, Valencia.

Contact Information

Olivier.dumont@ulg.ac.be

0032498226404

Definitions/Abbreviations

A	Area [m2]
b	Axial chord of the blades [m]
CHP	Combined Heat and Power
D	Diameter at mid-height of the blades [m]
f	Coefficient [-]
h	Enthalpy [J/(kg)]
K	First velocity coefficient [-]
k	Loss coefficient [-]
$\dot{m}$	Mass flow rate [kg/s]
N	Shaft speed [RPM]
oh	Overheating [K]
P	Pressure [bar]
pr	Pressure ratio [-]
r	Radius [m]
s	Blade spacing [m]
t	Temperature [°C]
U	Absolute speed of the blades [m/s]
V	Absolute speed of the fluid [m/s]
$\dot{W}$	Power [W]
Greek	
α	Absolute orientation of the fluid
β	Relative orientation of the fluid
ρ	Density [kg/m3]
η	Efficiency [-]
ε	Ratio [-]
σ	Second velocity coefficient [-]
ω	Angular speed [rad/s]
Indices	
AC/DC	inverter
el	electrical
ex	exhaust
exp	expander
f	leakage
gen	generator
in	inlet
is	isentropic
loss	loss
meas	measured
pred	predicted
red	reduced
rot	rotor
s	entropic
TT	total

Appendix

Table A1. Technical data of the sensors

Measure	Position	Sensor type	Range	Accuracy
Temperature	1	Thermocouple (K)	[0-1200]°C	2.5 K
	2	Thermocouple (K)	[0-1200]°C	2.5 K
	3	Thermocouple (T)	[0:260]°C	1K
	4	Thermocouple (T)	[0:260]°C	1K
	5	Thermocouple (K)	[0-1200]°C	2.5 K
	6	Thermocouple (T)	[0:260]°C	1K
	7	Thermocouple (T)	[0:260]°C	1K
	8	Thermocouple (T)	[0:260]°C	1K
	+	Thermocouple (T)	[0:260]°C	1K
	10	Thermocouple (T)	[0:260]°C	1K
	11	Thermocouple (T)	[0:260]°C	1K
	room	Thermocouple (T)	[0:260]°C	1K
Pressure	1-2	Difference	[0:1.6] bar	0.0016 bar
	2	Absolute	[0:0.5] bar	0.0025 bar
	4	Absolute	[0:25] bar	0.125 bar
	4-5	Difference	[0:1.6] bar	0.0016 bar
	5	Absolute	[0:25] bar	0.125 bar
	6	Absolute	[0:20] bar	0.2 bar
	7	Absolute	[0:6] bar	0.06 bar
Engine torque	A	Force sensor	[0:700] Nm	0.3 Nm
Engine speed	A	Pulse encoder	[0:15 000] RPM	30 RPM
Air-fuel ratio	A	λ probe	-	0.1
Gasoline flow rate	A	Coriolis	[0.3:60] kg/h	0.6 kg/h
Water flow rate	4	Coriolis	[0:25] g/s	0.1 g/s
Turbine speed	G	Pulse encoder	[0:30 000] RPM	500 RPM
Turbine power (1st wheel)	G	Wattmeter	[0:2000] W	10 W
Turbine power (2nd wheel)	G	Wattmeter	[0:2000] W	10 W